



Contents lists available at ScienceDirect

International Journal of Rock Mechanics and Mining Sciences

journal homepage: <http://www.elsevier.com/locate/ijrmms>

Stress perturbation caused by multistage hydraulic fracturing: Implications for deep fault reactivation

Mengke An^{a,b}, Fengshou Zhang^{a,b,*}, Egor Dontsov^c, Derek Elsworth^{d,e}, Hehua Zhu^{a,b}, Luanxiao Zhao^f

^a Department of Geotechnical Engineering, College of Civil Engineering, Tongji University, Shanghai, 200092, China

^b Key Laboratory of Geotechnical & Underground Engineering of Ministry of Education, Tongji University, Shanghai, 200092, China

^c ResFrac Corporation, Palo Alto, CA, 94301, USA

^d Department of Energy and Mineral Engineering, EMS Energy Institute and G3 Center, The Pennsylvania State University, University Park, PA, 16802, USA

^e Department of Geosciences, The Pennsylvania State University, University Park, PA, 16802, USA

^f State Key Laboratory of Marine Geology, Tongji University, Shanghai, 200092, China

ARTICLE INFO

Keywords:

Shale reservoir
Induced seismicity
Hydraulic fracturing
Stress perturbation
Fault reactivation
Dislocation theory

ABSTRACT

Swarms of earthquakes during shale gas exploitation in the Changning area of Sichuan Basin indicate that hydraulic fracturing induces seismicity both within the target reservoir but also to depths of several kilometers below the horizontal well. These remote earthquakes are possibly triggered by total stress perturbations resulting from the hydraulic fracturing. We use a dislocation-based analytical model to simulate multistage hydraulic fracturing of three horizontal wells at a single well pad to explore the spatiotemporal evolution of total stress perturbations. Results show that the number and distribution of fracturing stages affect both the distribution and magnitude of stress changes and that the stress change diminishes with distance. The undrained injection-induced stress change is below 10^{-3} MPa at distances ≥ 1 km for first-stage fracturing but reach 10^{-1} MPa for multistage fracturing of 30 stages in three wells. Undrained stress changes scale linearly with the magnitude of fluid leakoff into the formation – halving the effective fracture width halves the induced stress magnitudes and with an identical distribution – limiting the potential for fault reactivation. Scaling analysis for pressure diffusion distal from the reservoir indicate that the short-term impact is indeed essentially undrained. Estimates for long-term depletion identify a similar induced stress signal of opposite sign but with similar Coulomb potential for reactivation in the long-term. Such magnitudes of Coulomb stress changes suggest the possibility of fault reactivation on critically-stressed faults at kilometer separation from the injection both in the short-term due to stimulation and in the long-term resulting from depletion.

1. Introduction

The Sichuan Basin of southwest China is one of the major shale gas production areas in China. Development of this resource has drawn significant attention in recent years due to the sudden increase in the triggering of small to mid-sized earthquakes associated with the shale gas exploitation.^{1–6} Temporary monitoring stations (Fig. S1) deployed in the Changning national shale gas demonstration area of the southern Sichuan Basin (coordinates: N28°–28.4° and E104.6°–105°) recorded swarms of $M_L \geq 1.0$ earthquakes in 2017 (Fig. 1). The number of earthquakes shows a unimodal distribution with depth (Fig. 2a) with a peak located at ~ 2.0 km. This peak is within the depth range of the

lower Silurian Longmaxi formation, the major target shale gas reservoir layer in the Sichuan Basin^{7,8}. The maximum earthquake magnitudes are $M_L \sim 4.5$ within 4.0 km and $M_L \sim 4.7$ within 10.0 km (Fig. 2b). These events are temporally correlated with hydraulic fracturing operations and suggest the reactivation of pre-existing subsurface faults.^{9–12}

Significant effort has been devoted towards understanding potential mechanisms of seismicity induced during hydraulic fracturing related geo-energy recovery, including those for the recovery of shale gas and deep geothermal energy and for saltwater disposal.^{13–16} It is widely accepted that the injection of fluids at high-pressure reduces effective strength and promotes fault stress drop and reactivation.^{6,17–21} This partly explains how hydraulic fracturing at the depth of the Longmaxi

* Corresponding author. Department of Geotechnical Engineering, College of Civil Engineering, Tongji University, Shanghai, 200092, China.

E-mail address: fengshou.zhang@tongji.edu.cn (F. Zhang).

<https://doi.org/10.1016/j.ijrmms.2021.104704>

Received 15 September 2020; Received in revised form 2 February 2021; Accepted 10 March 2021

1365-1609/© 2021 Elsevier Ltd. All rights reserved.

formation induces the largest number of earthquakes (Fig. 2a). However, deeper clusters remain enigmatic. These earthquakes can only be directly triggered by the fluid injection if there are active fluid conduits providing rapid connectivity with the reservoir.^{17,22} To the contrary, observations show the Longmaxi formation to be dense with a low porosity and extremely low permeability.^{23,24} Based on these field observations,^{1,2,25} we postulate that these unexplained earthquakes, several kilometers below the injection formation, are associated with the presence of three enabling features. First, the underlying strata below the Longmaxi formation are structurally complex and potentially tectonically-active with several large-scale thrust faults apparent (Fig. 3). Second, the underlying strata, comprising tectosilicate-rich sandstone and carbonate-rich dolomite or limestone, make these pre-existing faults potentially frictional unstable at *in-situ* conditions.²⁶⁻²⁹ And third, and most importantly, the total stress perturbation driven by multistage hydraulic fracturing in the distant Longmaxi formation is sufficient to trigger pre-existing faults at the underlying strata. It has been demonstrated that stress changes from hydraulic fracturing may activate fault reactivation at distances of >1 km.^{9,30}

Defining the Coulomb failure stress resulting from a prescribed injection perturbation is a common procedure to assess fault reactivation potential.³¹⁻³³ Shear reactivation results when the Coulomb shear traction τ acting on the fault plane is larger than its shear strength τ_s , as,

$$\tau - \tau_s = \tau - (\mu_s \cdot \sigma_n^{eff} + C_0) \geq 0 \quad (1)$$

where C_0 is the cohesion (usually equals to zero for mature gouge-filled pre-existing faults), μ_s is the static frictional coefficient of the fault, and σ_n^{eff} is the effective normal stress acting on the fault plane. To evaluate whether a fault is advancing towards of retreating from failure, the change in Coulomb failure stress (ΔCFS) as a function of normal and shear stress is defined as,³⁴

$$\Delta CFS = \Delta\tau - \mu_s \cdot (\Delta\sigma_n - \Delta P) = \Delta\tau - \mu_s \cdot \Delta\sigma_n^{eff} \quad (2)$$

where $\Delta\tau$, $\Delta\sigma_n$, ΔP , and $\Delta\sigma_n^{eff}$ are the changes in shear stress, normal stress, pore pressure and effective normal stress, respectively. A fault shows a higher potential for reactivation when ΔCFS is positive, especially for critically-stressed faults. Earthquakes can be triggered at ΔCFS s as low as 0.01 MPa.³⁵⁻³⁷ Coulomb failure stress changes proximal to injection during shale gas hydraulic fracturing in the Sichuan Basin are known to be greater than 0.1 MPa² – enabling ready reactivation. However, the characteristics of stress perturbations distant from injection remain unknown.

To define the potential for remote reactivation of faults, we define the magnitude and sense of distal perturbations on Coulomb stress at different reservoir depths that result from multistage hydraulic fracturing. We use these characterizations to define the reactivation potential of pre-existing critically-stressed faults. We follow typical hydraulic fracturing injection schedules for field operations in the Sichuan Basin to define Coulomb stress changes using dislocation-based

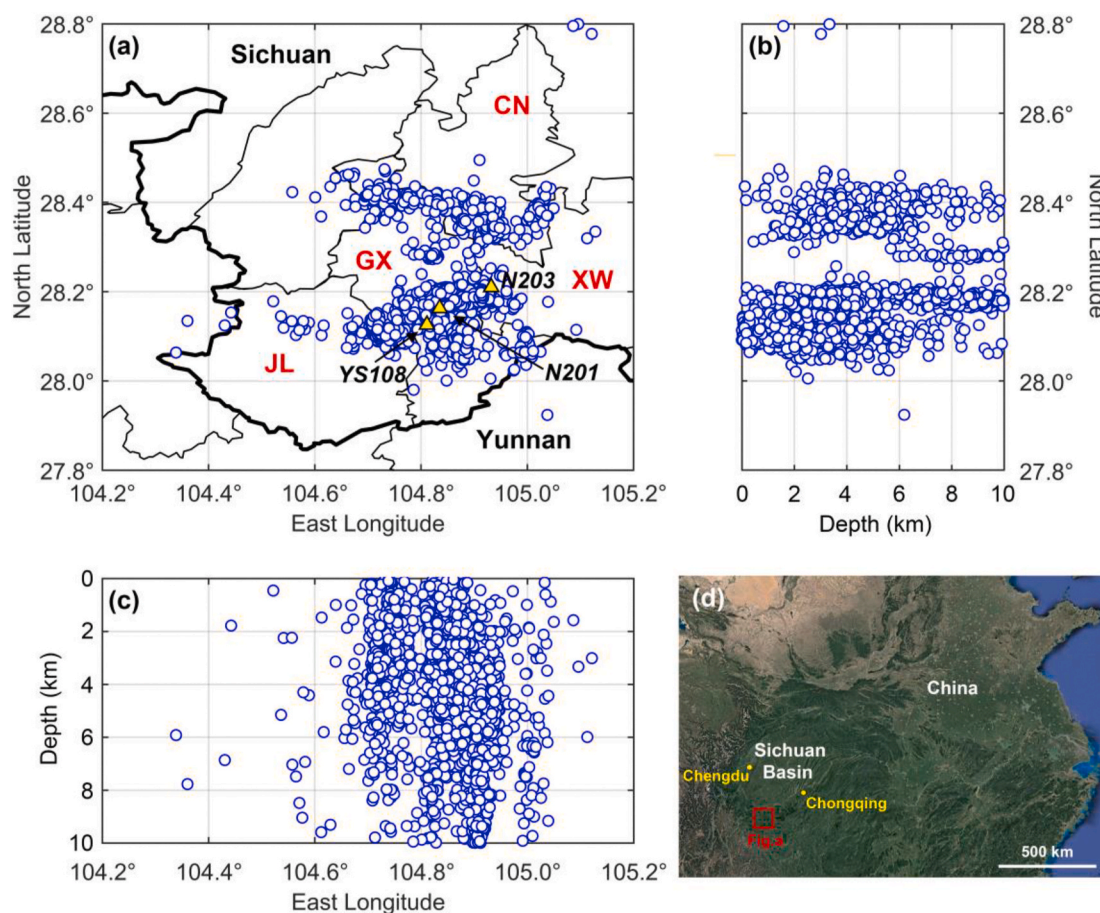


Fig. 1. Earthquake distribution in the Changning area, Sichuan Basin, southwest China. (a) Distribution of $M_L \geq 1.0$ earthquakes (blue circles) in 2017 in the Changning area (coordinates: E104.2°–105.2°, N27.8°–28.8°). The yellow triangles denote the three exploration wells (N203, N201 and YS108). The thick black solid line is the provincial boundary (Sichuan and Yunnan Province) and the thin black solid lines are county boundaries. CN = Changning county, GX = Gaoxian county, XW = Xingwen county, and JL = Junlian county. The relationships of earthquake depth with latitude (north) and longitude (east) are shown in (b) and (c), respectively. (d) The location of the Changning block (red triangle) and the Sichuan Basin. The Changning block is located at the southern part of the Sichuan Basin (red square). The two yellow circles denote the two large cities of Chengdu and Chongqing in southwest China. The earthquake data were derived from .⁵ (For interpretation of the references to color in this figure legend, the reader is referred to the Web version of this article.)

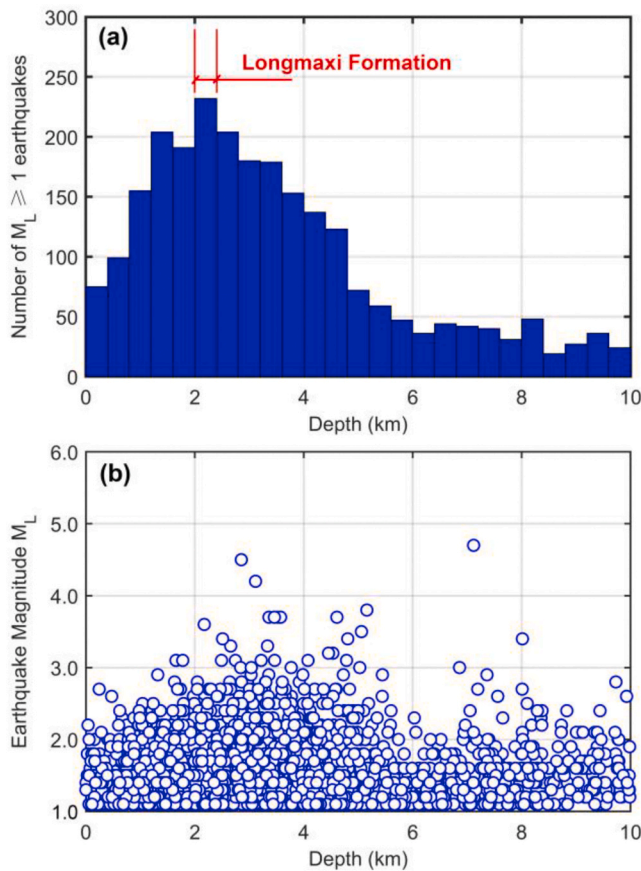


Fig. 2. Earthquake frequency and magnitude in the Changning area. (a) Number of $M_L \geq 1.0$ events with depth in 2017. Zero depth represents sea level. (b) The relationship of earthquake magnitude and depth in 2017.

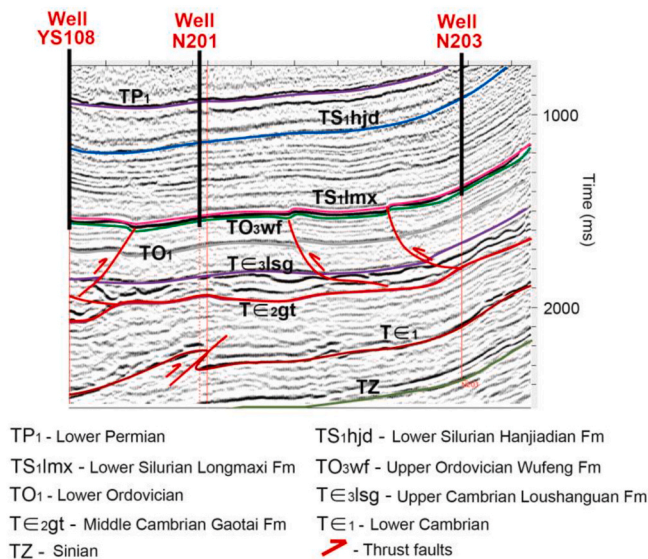


Fig. 3. Seismic reflection profile showing the tectonic setting of the Changning area in a section through three exploration wells (YS108, N201, and N203) (modified from .²⁹ The colored solid lines represent the base of strata and formations.

methods. These analyses define the spatiotemporal distributions of stress changes during a multistage hydraulic fracturing job and define the ability of the stress perturbations to reactivate deep critically-

stressed faults at different depths below the injection point.

2. Modeling methods

A plan view of the multi-stage fracturing model is shown in Fig. 4a. The model includes a single pad consisting of three parallel horizontal wells following the typical well configuration in the Changning area of the Sichuan Basin. Each well has 30 fracturing stages in its total horizontal length of 1500 m and each stage has three fracturing clusters. The stage spacing is 50 m, the well spacing is 500 m and each hydraulic fracture is represented by a symmetric bi-wing fracture of 200 m in length and 100 m in height. A total of 1920 m³ fluid (including 1800 m³ water and 120 m³ sand) is injected for each fracturing stage. Although up to three hydraulic fractures can be initiated in each stage, we assume a single fracture plane in each fracturing stage by combining all potential fractures into a single equivalent fracture (length of 400 and height of 100 m) (Fig. 4b). The well length, spacing, and fluid injection volume are selected from the field operation data for the Sichuan Basin. Fracture size is estimated from microseismic observations.^{57,38} Adopting a fracture size of 400 m × 100 m and assuming an injected volume of 1920 m³ yields an upper bound for the average fracture width (*w*) of 4.8 cm - this assumes no fluid leak-off and a uniform fracture width. We utilize this fracture aperture of 4.8 cm for each stage to investigate the upper limit of the distal stress perturbation. The hydraulic fracturing was performed at the Longmaxi shale reservoir layer which has the burial depth of ~2500 m. The origin of the coordinate system is placed at the injection point of the first stage of the central well (well 1) (yellow circle in Fig. 4) and the three wells are aligned along the y axis. The elastic modulus (*E*) of the reservoir is taken as 40 GPa and the Poisson's ratio (ν) is 0.2. The dislocation theory used for the stress calculation is described in Appendix A and all calculations are performed using the MATLAB.

3. Results

We calculate the distal total stress changes for different hydraulic fracturing geometries and schedules following the method described in Appendix A. The results for two specific scenarios are selected - that for first-stage fracturing and for multi-stage fracturing - as detailed below.

3.1. Distribution of stress change due to the first hydraulic fracturing stage

We first analyze the effect of first-stage fracturing on the stress change at different reservoir depths. The contours of stress components S_{xx} , S_{yy} and S_{zz} after the fracturing of the first stage of well 1 at depths of $z = -1$ km and -2 km are shown in Fig. 5. A horizontal area of 4000 m × 8000 m is chosen to display the results. The magnitude of the stress change at $z = -1$ km is in the range of 10^{-4} - 10^{-3} MPa, higher than that at $z = -2$ km where it is in the range 10^{-5} - 10^{-4} MPa - defining the rate of stress drop with distance.

Positive stress change represents compression with the contours of the stress component S_{xx} (Fig. 5a and d) indicating that a zone of compression is formed around the injection point and that it extends along the x axis. Four zones of extension are induced at the upper, bottom, left and right positions and four complementary zones of compression develop at the diagonal positions (Fig. 5a and d). Conversely, extensional zones are generated around the origin of the coordinate system in terms of stress components S_{yy} and S_{zz} (Fig. 5b, c, 5e and 5f) as a result of the first fracturing stage. Simultaneously, compressive zones are induced at the upper and lower positions of the extensional zones in Fig. 5b, c, 5e and 5f. From Fig. 5, the zones of induced extension or compression at $z = -2$ km are much larger than that at $z = -1$ km. This confirms that the stress decays gradually along the z axis as a result of the first fracturing stage.

Variation of the fracturing-induced stresses S_{xx} , S_{yy} , S_{zz} , S_{yz} , S_{xz} and S_{xy} along the y axis due to the first fracturing stage of well 1 at $z = -1$ km

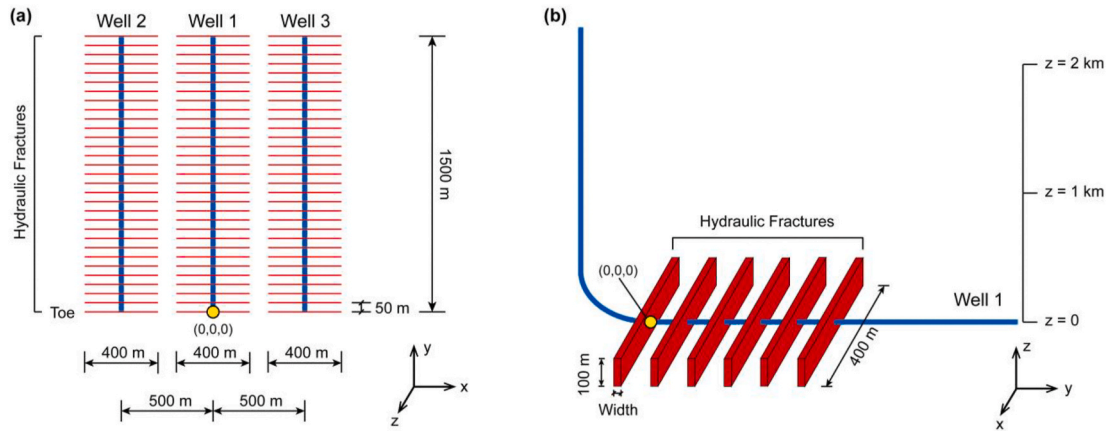


Fig. 4. (a) Plan view (XY plane) of the model with three horizontal wells and thirty fractures per well. (b) 3D view of the central well (well 1).

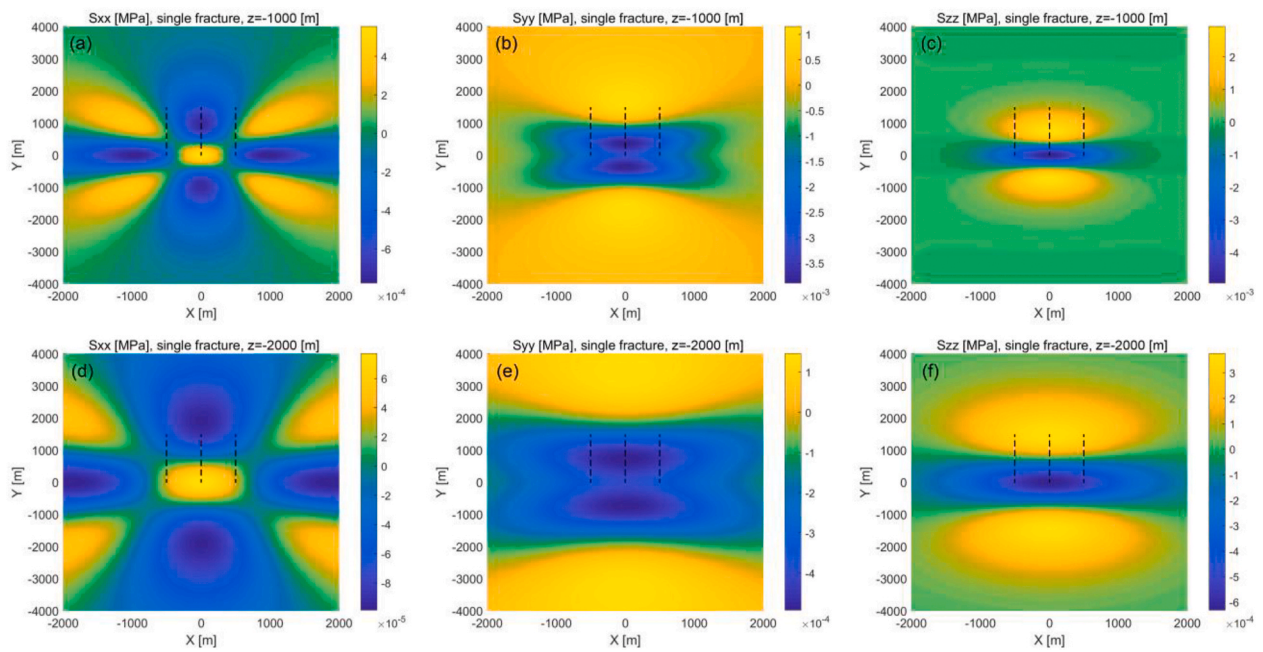


Fig. 5. Contours of induced stresses S_{xx} , S_{yy} and S_{zz} as a result of the first fracturing stage of well 1 at depths of $z = -1$ km (top) and -2 km (bottom). The origin, $z = 0$, is set at the elevation of the wells with negative z values corresponding to depth below the horizontal wells (Fig. 4). Distribution of changes in stresses (a) S_{xx} at $z = -1000$ m, (b) S_{yy} at $z = -1000$ m, (c) S_{zz} at $z = -1000$ m, (d) S_{xx} at $z = -2000$ m, (e) S_{yy} at $z = -2000$ m, and (f) S_{zz} at $z = -2000$ m. The black dashed lines indicate the locations of three fracturing wells.

and -2 km is shown in Fig. 5. Stresses S_{xz} and S_{xy} are only marginally affected by the hydraulic fracturing and remain unchanged (Fig. 6). Changes in S_{xx} , S_{yy} , S_{zz} along the y axis are symmetric about the origin for both $z = -1$ km and -2 km, which is in agreement with the contours shown in Fig. 5. The stress change of S_{yz} is antisymmetric about the origin for both depths. The maximum stress change along the y axis in Fig. 6 corresponds to the component S_{zz} . At the center of the first fracturing stage ($y = 0$), the stress S_{zz} has decreased by $\sim 5 \times 10^{-3}$ MPa at $z = -1$ km and $\sim 6 \times 10^{-4}$ MPa at $z = -2$ km. Reductions in the stress components S_{yy} and S_{yz} are smaller than those in S_{zz} at both depths, while the smallest variation is observed for S_{xx} . Stress S_{zz} along the y axis shows the maximum compressive values, with the magnitude reaching $\sim 3 \times 10^{-3}$ MPa at $z = -1$ km and $\sim 4 \times 10^{-4}$ MPa at $z = -2$ km, followed by the stress components S_{yz} , S_{zz} and S_{xx} . From Fig. 6, the volume affected by the first fracturing stage at the heel of the first well is mainly within the range of $-3000 \text{ m} \leq y \leq 3000 \text{ m}$.

3.2. Distribution of stress changes due to multistage fracturing

“Zipper fracturing” is typically implemented from a single well pad – fractures are initiated alternately in adjacent wells, advancing along the well like teeth merging as a zipper is closed. For simplicity, we assume that all three horizontal wells (Fig. 4) are fractured simultaneously with the same schedule, i.e., all fractures in the three horizontal wells are added instantaneously. The region of investigation is confined within a horizontal area of $2000 \text{ m} \times 4000 \text{ m}$. Contours of stress changes of S_{xx} , S_{yy} and S_{zz} following the fracturing of these 30 stages on each of the three wells at depths of $z = -1$ km and -2 km are shown in Fig. 7. The magnitude of the stress change in Fig. 7 varies from the order of 10^{-2} to 10^{-1} MPa at $z = -1$ km and from the order of 10^{-3} to 10^{-2} MPa at $z = -2$ km. These are proportionally much higher than that due to the first fracturing stage on well 1 due to the ninety-fold increase in the total volume of injection (Fig. 5).

In contrast to the case for the first fracturing stage, the resulting induced stress distribution for multistage fracturing is significantly more

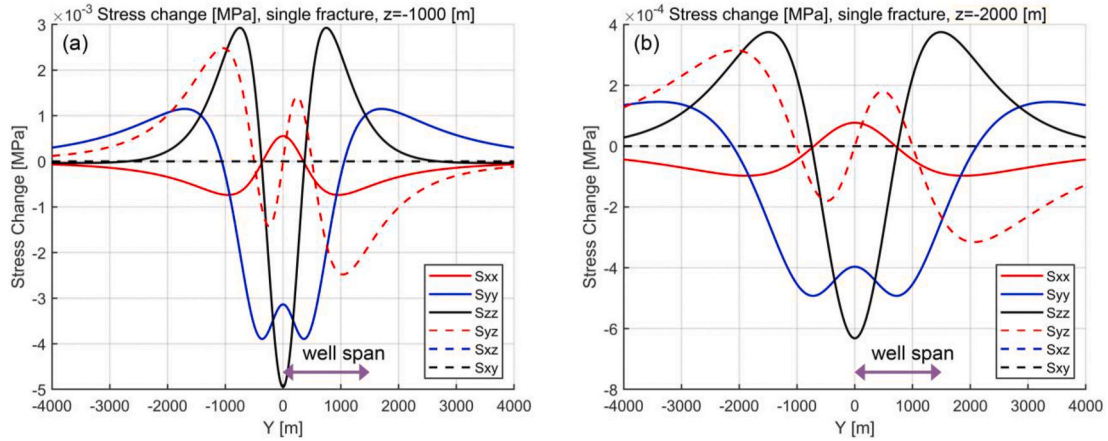


Fig. 6. Variation of stress components S_{xx} , S_{yy} , S_{zz} , S_{yz} , S_{xz} and S_{xy} along the y axis due to the fracturing of stage 1 on well 1 at depths of (a) $z = -1$ km and (b) $z = -2$ km. Negative z values indicate depth below the horizontal fracturing well. The arrow represents the well span along the y direction.

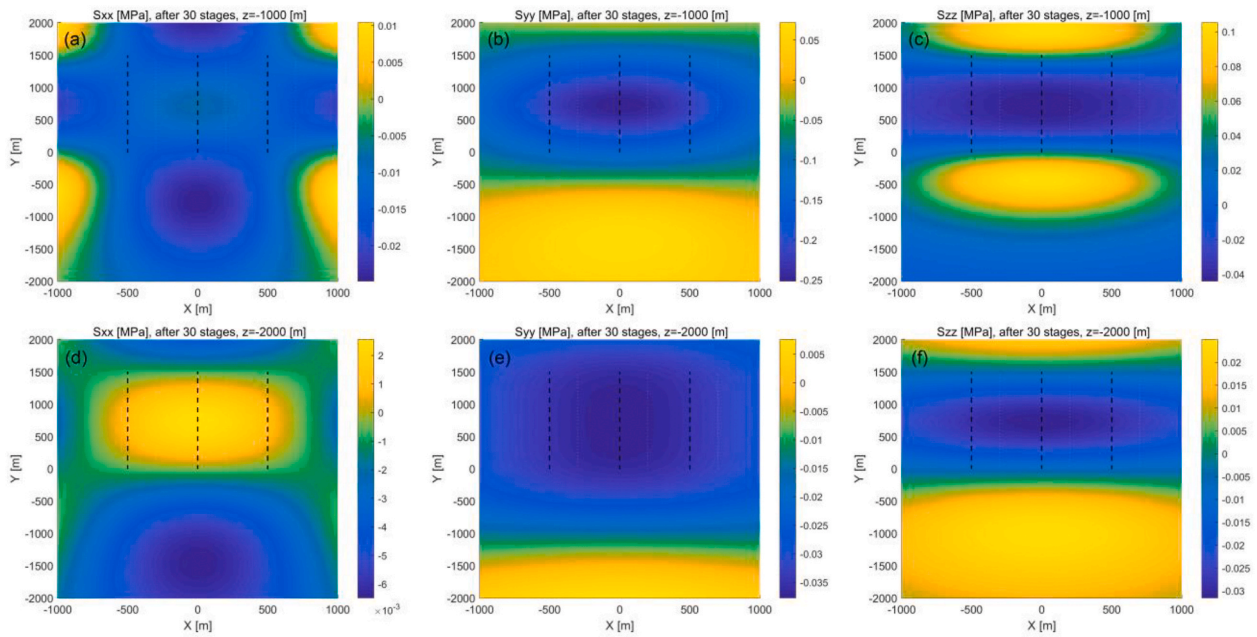


Fig. 7. Contours of stress components S_{xx} , S_{yy} and S_{zz} due to fracturing of 30 stages on each of the three horizontal wells at depths of $z = -1$ km (top) and $z = -2$ km (bottom). Negative values of z indicate depth below the horizontal fracturing wells. Distribution of changes in stresses (a) S_{xx} at $z = -1000$ m, (b) S_{yy} at $z = -1000$ m, (c) S_{zz} at $z = -1000$ m, (d) S_{xx} at $z = -2000$ m, (e) S_{yy} at $z = -2000$ m, and (f) S_{zz} at $z = -2000$ m. The black dashed lines indicate the locations of three fracturing wells.

complex due to the accumulation of stress perturbations from multiple sources distributed spatially along the wells. The compressive zones (yellow colors) are distributed further away from the wells in terms of the stress component S_{xx} at $z = -1$ km (Fig. 7a) and an extensional zone (dark blue contour) is formed at $-500 \text{ m} \leq x \leq 500 \text{ m}$ and $-1500 \text{ m} \leq y \leq 0 \text{ m}$. At $z = -2$ km (Fig. 7d), a compressive zone is formed directly under the wells at $0 \text{ m} \leq y \leq 1500 \text{ m}$, while an extensional zone is located below at $-2000 \text{ m} \leq y \leq -500 \text{ m}$ – this is also apparent above the wells, due to symmetry. For the stress change in S_{yy} at $z = -1$ km (Fig. 7b), extensional and compressional zones are observed in the range of $0 \text{ m} \leq y \leq 1500 \text{ m}$ and $-2000 \text{ m} \leq y \leq -1500 \text{ m}$, respectively. However, at $z = -2$ km (Fig. 7e), the extensional zone expands over the range of $-500 \text{ m} \leq y \leq 2000 \text{ m}$ and the area of the compressive zone is reduced over the region of $-2000 \text{ m} \leq y \leq -1500 \text{ m}$. In Fig. 7c, two compressional zones are identified between $1500 \text{ m} \leq y \leq 2000 \text{ m}$ and $-1000 \text{ m} \leq y \leq -500 \text{ m}$ for the stress component S_{zz} at $z = -1$ km, with an extensional zone between. At $z = -2$ km in Fig. 7f, the range of the extensional zone is near identical to that at $z = -1$ km, but the lower zone of compression expands in the

range of $-2000 \text{ m} \leq y \leq 0 \text{ m}$ with the upper compressional zone only apparent near $y = -2000 \text{ m}$.

Fig. 8 shows fracturing-induced variations in the components S_{xx} , S_{yy} , S_{zz} , S_{yz} , S_{xz} and S_{xy} along the y axis for the multistage fracturing on each of the three wells at depths of $z = -1$ km and -2 km. Similar to the results for a single fracturing stage on well 1 (Fig. 6), the stresses S_{xy} and S_{xz} remain zero. The maximum stress change corresponds to reductions in the magnitude of S_{yy} in the range of $500 \text{ m} \leq y \leq 1000 \text{ m}$ in Fig. 8, with this reduction reaching ~ 0.25 MPa at $z = -1$ km and ~ 0.04 MPa at $z = -2$ km. At $z = -1$ km, the reductions in S_{yz} , S_{xx} and S_{zz} are less than 0.15 MPa (Fig. 8a). However, the maximum reduction in S_{zz} is much less than that of S_{yy} with the smallest values corresponding to stresses S_{xx} and S_{yz} at $z = -2$ km (Fig. 8b). The maximum stress increases are observed for components S_{yz} and S_{zz} , with ~ 0.125 MPa at $z = -1$ km and ~ 0.025 MPa at $z = -2$ km. The changes in components S_{xx} , S_{yy} and S_{zz} are symmetric about the line $y = 725 \text{ m}$ and the changes in component of S_{yz} are antisymmetric about the same line.

To investigate the temporal evolution of the stress variations, we

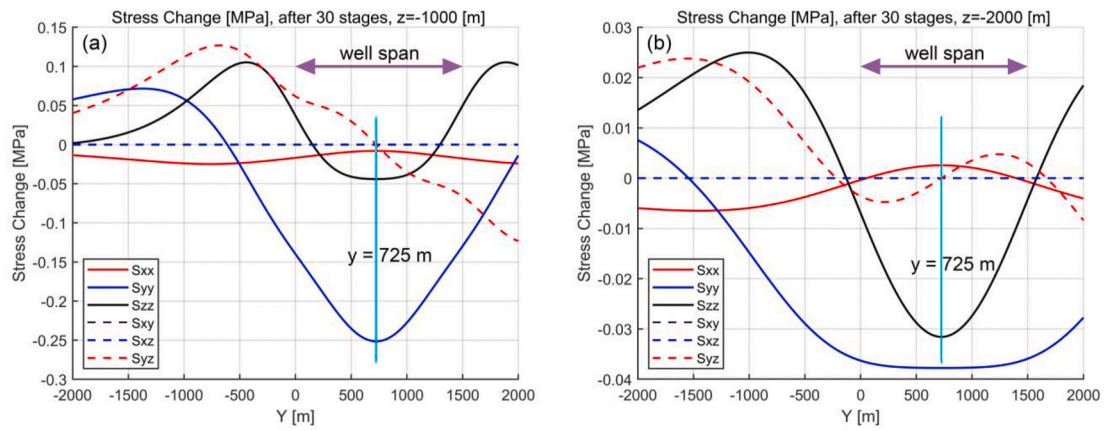


Fig. 8. Variation in stress components S_{xx} , S_{yy} , S_{zz} , S_{xz} and S_{yz} along the y axis for the case of fracturing of 30 stages on each of three horizontal wells at depths of (a) $z = -1$ km and (b) $z = -2$ km. Negative values of z indicate depth below the horizontal fracturing wells. The arrow represents the well span along the y direction and the solid cyan line denotes $y = 725$ m. (For interpretation of the references to color in this figure legend, the reader is referred to the Web version of this article.)

compare the changes in S_{xx} , S_{yy} and S_{zz} along the y axis for the cases of 1, 10, 20 and 30 fracturing stages on each of the three horizontal wells – all three wells are fractures simultaneously and instantaneously. This approximates the temporal response, with the results presented in Fig. 9. Fracturing-induced stress increases with an increase in the number of fracturing stages at both depths, except for the changes of S_{zz} at $z = -1$ km. This implies that the number of the fracturing stages (or the total volume pumped) plays an important role in controlling the distribution of the stress perturbation at different reservoir depths. Within the range of the well span ($0 \leq y \leq 1500$ m), S_{xx} shows the largest increase for the different number of fracturing stages at both depths, while both S_{yy} and S_{zz} exhibit the largest decrease.

4. Discussion

4.1. Effect of fracture width

The above results are presented for the case of the maximum possible fracture width ($w = 4.8$ cm) by assuming zero leakoff. Here we incorporate the effect of fluid leak-off and explore the stress changes for the different number of fracturing stages placed on three horizontal wells. First, a half-maximum fracture width ($w = 2.4$ cm) is adopted. Fig. 10 shows the stress variations in terms of components S_{xx} , S_{yy} , and S_{zz} along the y axis for different numbers of fracturing stages on three horizontal wells at depths of $z = -1$ km and -2 km. Compared with the results for the maximum fracture width ($w = 4.8$ cm, Fig. 9), the trends in the distribution of stress for the half-maximum fracture ($w = 2.4$ cm) due to different fracturing stages are identical – but magnitudes are halved – consistent with the linearity of governing equations 8–16 (Appendix A) where each stress component is proportional to the magnitude of the

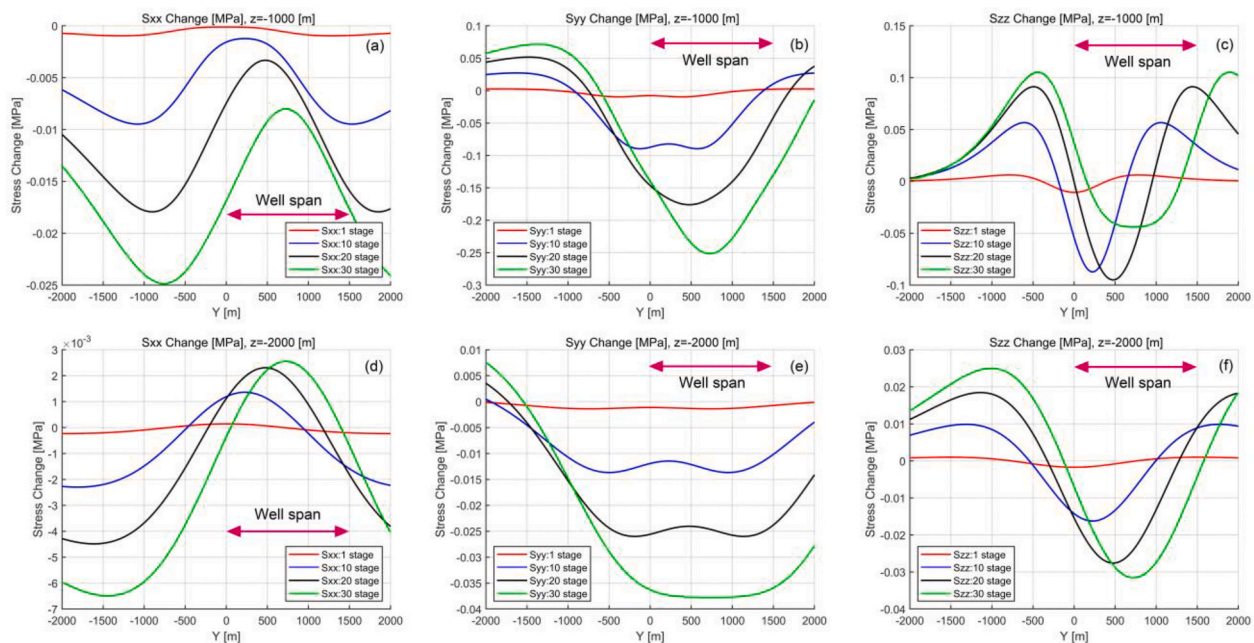


Fig. 9. Variation in stress components S_{xx} , S_{yy} and S_{zz} along the y axis for different numbers of fracturing stages (1, 10, 20 and 30) introduced simultaneously from the three horizontal wells at depths of (a) $z = -1$ km and (b) $z = -2$ km. Negative values of z indicate depths below the horizontal fracturing well. Distribution of changes in stresses (a) S_{xx} at $z = -1000$ m, (b) S_{yy} at $z = -1000$ m, (c) S_{zz} at $z = -1000$ m, (d) S_{xx} at $z = -2000$ m, (e) S_{yy} at $z = -2000$ m, and (f) S_{zz} at $z = -2000$ m. The arrow represents the well span along the y direction.

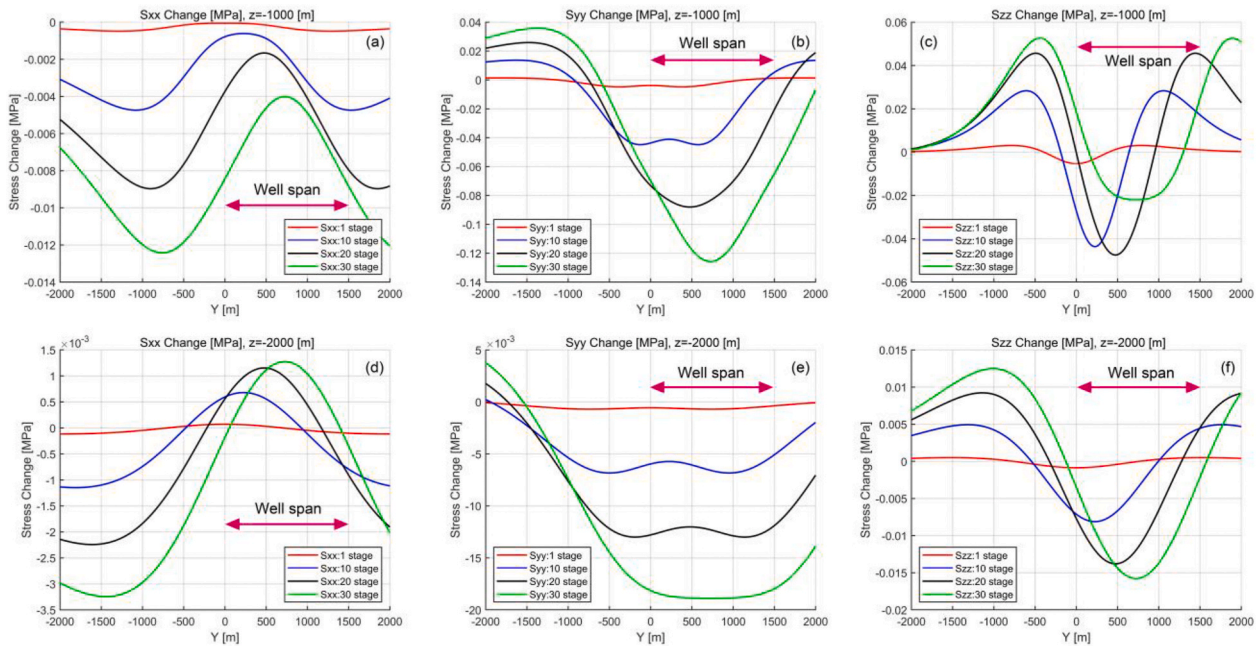


Fig. 10. Variation in stress components S_{xx} , S_{yy} and S_{zz} along the y axis for different numbers of fracturing stages (1, 10, 20 and 30) introduced simultaneously on the three horizontal wells to yield fracture widths of $w = 2.4$ cm and at depths of $z = -1$ km and -2 km. Negative values of z indicate the depths below the horizontal fracturing well. Distribution of changes in stresses (a) S_{xx} at $z = -1000$ m, (b) S_{yy} at $z = -1000$ m, (c) S_{zz} at $z = -1000$ m, (d) S_{xx} at $z = -2000$ m, (e) S_{yy} at $z = -2000$ m, and (f) S_{zz} at $z = -2000$ m. The arrow represents the well span along the y direction.

Burgers vector \mathbf{b} . This assumed reduced width of the fractures approximately represents the impact of fluid leakoff. This also suggests that the problem is intrinsically time dependent since leak-off gradually reduces fracture volume with time and therefore would also reduce the induced stresses. A large variation in fluid leakoff coefficient exists among different reservoir rock types. The Longmaxi formation typically consists of low permeability shales²⁴ with a low fluid leakoff coefficient. Thus the maximum-width fracture calculations therefore define the anticipated magnitude of the maximum induced stresses. Note that it is implicitly assumed in the above analysis that the fluid leakoff does not induce any further stress change in the reservoir, proximal to the fractures. However, the analysis in Ref. 39 demonstrates that this is not always the case. The leaking fluid elevates local pore pressures adjacent to the fractures,

which in turn induces an additional poroelastic stress. However, this stress is smaller than that of an open fracture with the same volume.

4.2. Effect of depletion

Production of oil and gas from shale reservoirs also leads to a significant decrease in reservoir pore fluid pressure. This can in turn result in a perturbation of the surrounding stresses acting within the reservoirs.^{40,41} While the hydraulic fracturing can be considered as a loading process with the injected pressurized fluids driving the opening and propagation of fractures, reservoir depletion can be characterized as this process in reverse – as unloading the reservoir. Here we compare the stress perturbations resulting from the depletion with those caused by

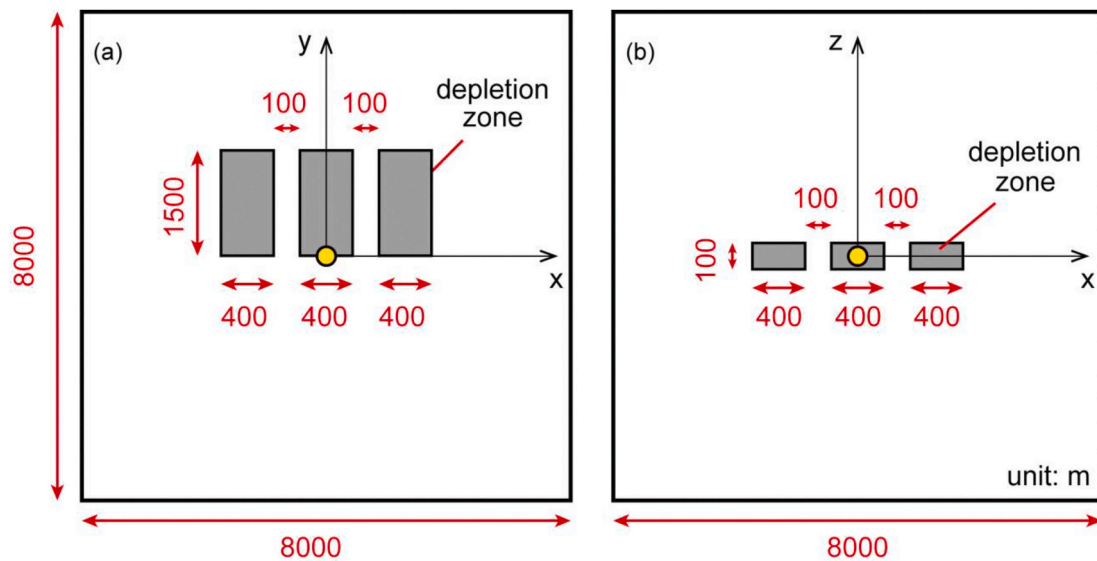


Fig. 11. Schematic of a prismatic depletion zone within a reservoir. (a) Side view of the xy -plane and (b) top view of the xz -plane. The yellow circles represent the origin of the coordinate system. (For interpretation of the references to color in this figure legend, the reader is referred to the Web version of this article.)

hydraulic fracturing. We employ theory of poroelasticity to predict the stress change resulting from reservoir depletion^{42,43} (details in Appendix B). It is assumed that the zone of depletion is prismatic with dimensions of $2a \times 2b \times 2c \text{ m}^3$. Solution for stresses induced by a depressurized prism can be found in Ref. 44 and as used in computing leak-off induced stresses by.³⁹ This calculation is also performed using MATLAB.

We consider an isotropic, porous and elastic reservoir ($8000 \times 8000 \times 8000 \text{ m}^3$) containing three embedded prismatic zones of depletion with dimensions of $400 \times 1500 \times 100 \text{ m}^3$ located in the center (Fig. 11). The origin of the coordinate system is placed at the heel of the central prismatic depletion zone. The dimensions of depletion zones are equivalent to the hydraulic fracturing zones (Fig. 4) enveloped by the span of the hydraulic fractures. The Biot coefficient is 0.6⁴⁵ and the uniform decrease of the pore pressure in the depletion zone is taken as 15 MPa. The elastic modulus and Poisson's ratio are taken as 40 GPa and 0.2, respectively. The changes in stresses S_{xx} , S_{yy} , S_{zz} , S_{xy} , S_{xz} and S_{yz} following reservoir depletion at depths of $z = -1 \text{ km}$ and -2 km are shown in Figs. 12 and 13, respectively. Resulting stress perturbations have orders of 10^{-2} MPa at $z = -1 \text{ km}$ and 10^{-3} MPa at $z = -2 \text{ km}$, similar to those after fracturing of the full 30 stages on three horizontal wells (Fig. 7). We do not accommodate the finite timescale for reservoir depletion, similar to not accommodating it in hydraulic fracturing estimates. However, reservoir depletion is intrinsically a long-term process and lasts for several years, while the timescale for hydraulic fracturing is relatively short and generally lasts only several months.⁴³ Thus, the estimates for depletion must be regarded as only and approximate representation.

4.3. Implications for deep fault behavior

We explore the impact of multistage fracturing on fault reactivation both proximal to and remote from the well system. As the magnitude of stress changes induced by multistage fracturing are larger than those for a first fracturing stage, we analyze the distribution of Coulomb failure stress (ΔCFS) only for this multistage case.

We consider a series of pre-existing faults that strike along the x axis, that dip in the y -direction with dip angles of 15° , 45° , and 75° . The static coefficient of friction is assumed to be 0.6. The fracturing-induced

changes in shear stress $\Delta\tau$ and normal stress $\Delta\sigma_n$ can be calculated at any point from the change in six stress components S_{xx} , S_{yy} , S_{zz} , S_{xy} , S_{xz} and S_{yz} . Figs. 14 and 15 show the distribution of Coulomb failure stress (ΔCFS) after the fracturing of 30 stages on three horizontal wells at depths of $z = -1 \text{ km}$ and -2 km , respectively. The studied region is the same as for Section 3.2. The maximum Coulomb failure stress (ΔCFS) reaches $\sim 0.2 \text{ MPa}$ at $z = -1 \text{ km}$ and $\sim 0.03 \text{ MPa}$ at $z = -2 \text{ km}$. The threshold Coulomb failure stress (ΔCFS) for the triggering earthquakes spans the range 0.01–0.05 MPa.^{46–48} Thus, the Coulomb failure stress (ΔCFS) induced by the fracturing of 30 stages on the three wells is sufficient to trigger seismicity at both depths (both within and below the reservoir, as observed). And this results from fracturing on only one well pad – when in reality multiple pads are near-simultaneously activated. The fault dip directions and magnitudes not only affect the distribution of the Coulomb failure stress (ΔCFS) but also influence its magnitude. For a given dip direction, the maximum Coulomb failure stress (ΔCFS) increases with an increase in dip magnitude for both depths.

Our modelling results have important implications for understanding fault stability behavior and induced seismicity in the Changning area. Current shale reservoir stimulation in the Changning area is mainly within the lower Silurian Longmaxi formation and at depths of 2–3 km. From previous studies,^{29,49} the Longmaxi formation shales are known to have a high content of phyllosilicate minerals and TOC (total organic carbon), enabling most shale faults to exhibit velocity-strengthening behavior and aseismic slip. The largest number of earthquakes in the Longmaxi formation (Fig. 2) highlights the importance of fault stress drop in triggering the earthquakes. The upper and lower formations of the Longmaxi shale, like the lower Silurian Shiniulan and upper Cambrian Xixiangchi formations, contain thick sandstone or dolomite. Both the tectosilicate-rich sandstone faults or the carbonate-rich dolomite faults are potentially unstable at *in-situ* conditions. The stress perturbations from the hydraulic fracturing in the Longmaxi formation are likely to reactivate the adjacent unstable sandstone or dolomite faults and trigger seismicity. These indicate that both the injection zone and adjacent brittle layers exhibit a high potential for seismicity during hydraulic fracturing.

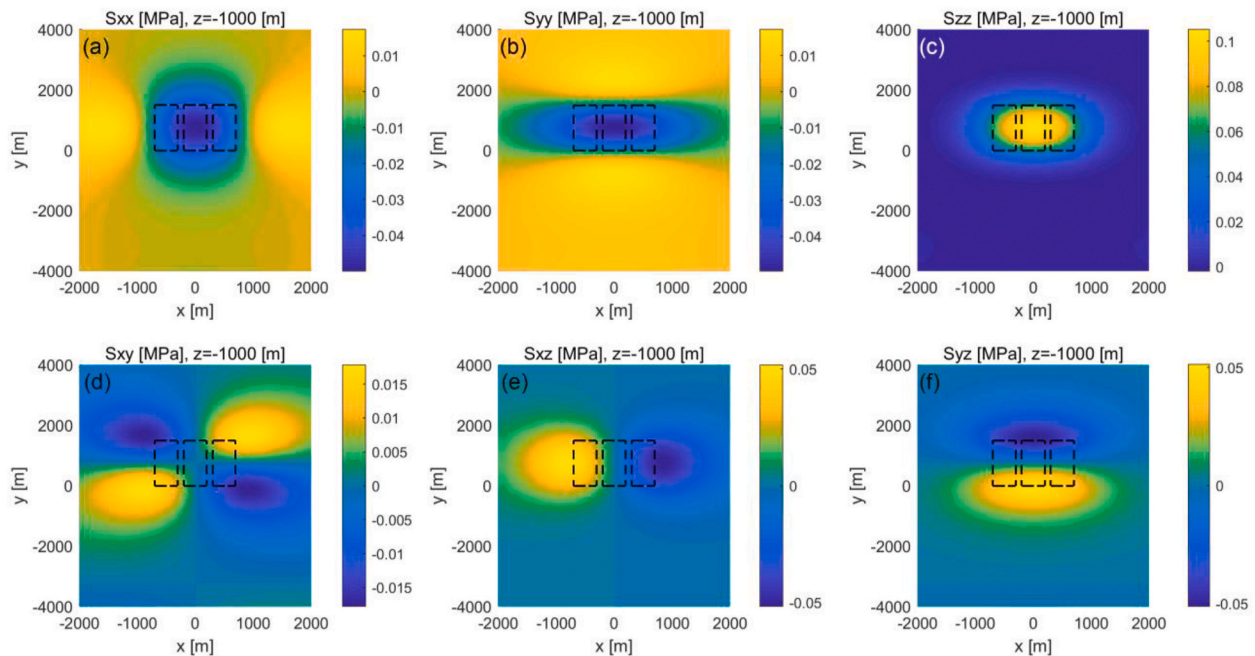


Fig. 12. Contours of stress changes in components (a) S_{xx} , (b) S_{yy} , (c) S_{zz} , (d) S_{xy} , (e) S_{xz} , and (f) S_{yz} after “ultimate” depletion at a depth of $z = -1 \text{ km}$. The dashed black triangles represent the depletion zones. Negative values of z indicate depths below the depletion zone.

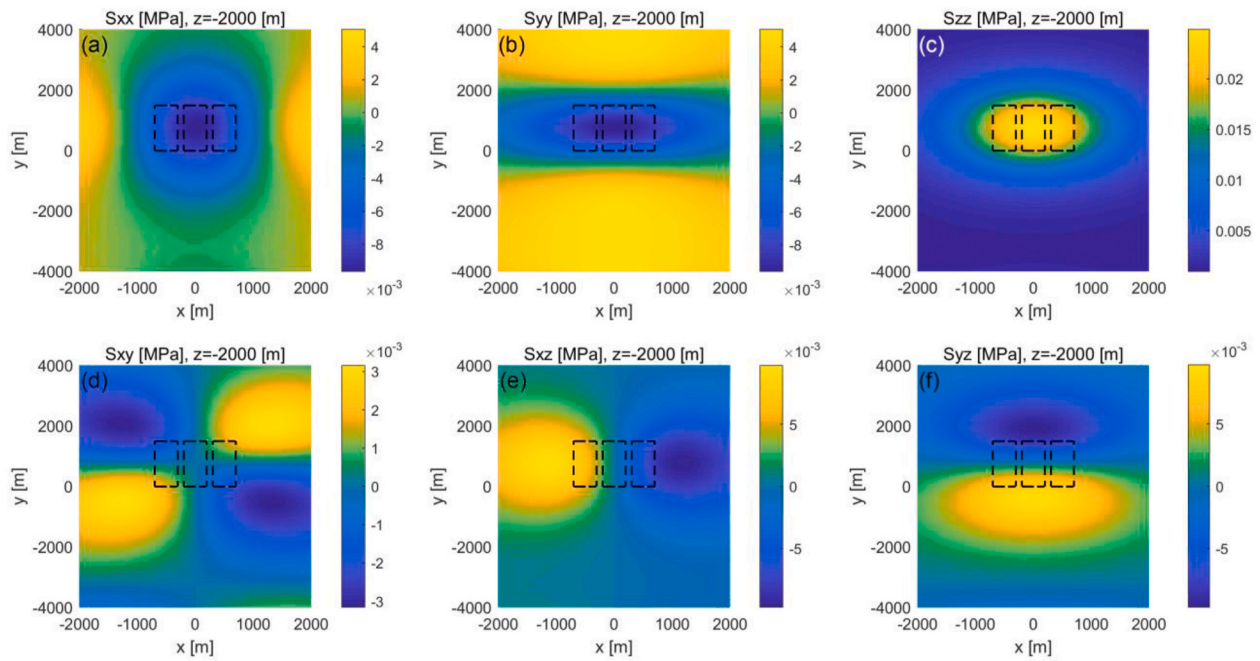


Fig. 13. Contours of stress changes in components (a) S_{xx} , (b) S_{yy} , (c) S_{zz} , (d) S_{xy} , (e) S_{xz} and (f) S_{yz} after “ultimate” depletion at a depth of $z = -2$ km. The dashed black triangles represent the depletion zones. Negative values of z indicate depths below the depletion zone.

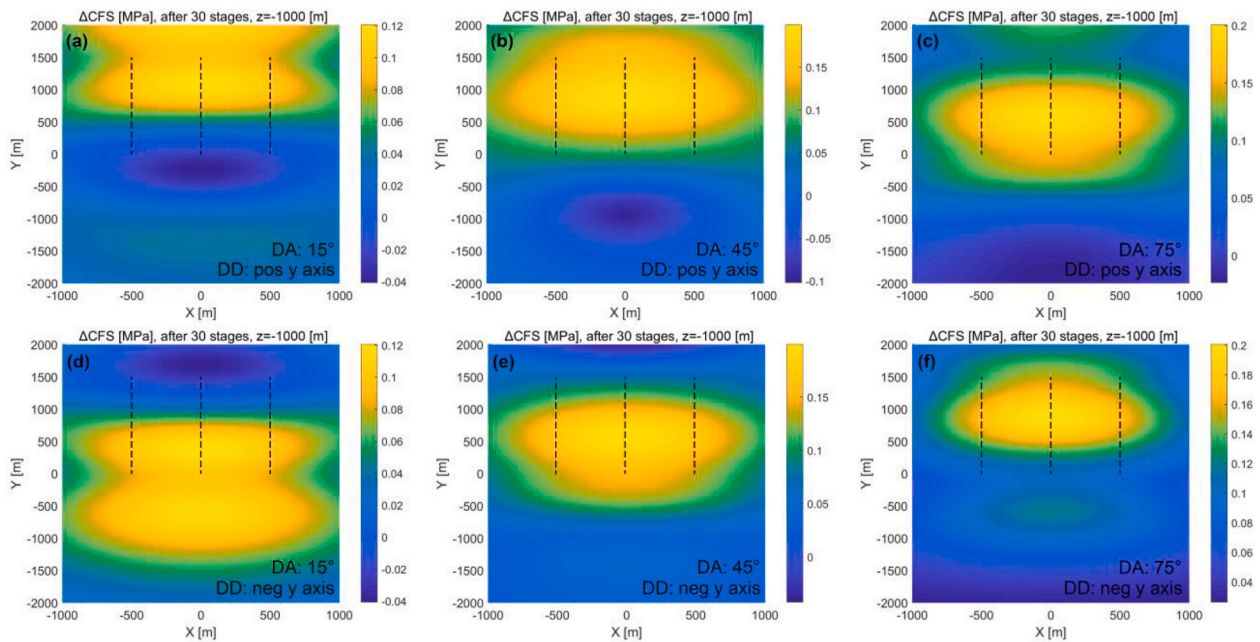


Fig. 14. Contours of Coulomb failure stress (ΔCFS) caused by the fracturing of 30 stages in all three wells at a depth of $z = -1$ km. Negative values of z indicate depth below the horizontal fracturing well. DA represents the dip angle and DD denotes the dip direction. Distribution of ΔCFS is shown for the following cases: (a) $DA = 15^\circ$ and DD in the positive y axis, (b) $DA = 45^\circ$ and DD in the positive y axis, (c) $DA = 75^\circ$ and DD in the positive y axis, (d) $DA = 15^\circ$ and DD in the negative y axis, (e) $DA = 45^\circ$ and DD in the negative y axis, and (f) $DA = 75^\circ$ and DD in the negative y axis. The black dashed lines indicate the locations of fracturing wells.

4.4. Effect of pore pressure increase on stress perturbation

An important question remains as to whether the pore pressure increase due to fracturing fluid diffusion can significantly affect the distal stress changes. Pore pressure increase has been shown to play an important role in triggering seismicity.^{15,47} The effects of pore pressure increase can be neglected if the timescale for loading is short and observations are in the near-term. The characteristic time t_c of diffusion^{42,50,51} may be expressed as,

$$t_c = \frac{L_c^2}{c}, \tag{3}$$

where L_c is the characteristic length of the pre-existing fault, c is the fluid diffusivity and can be calculated as,

$$c = k_m / \left(\frac{1}{M} + \frac{\alpha}{K + 4/3G} \right), \tag{4}$$

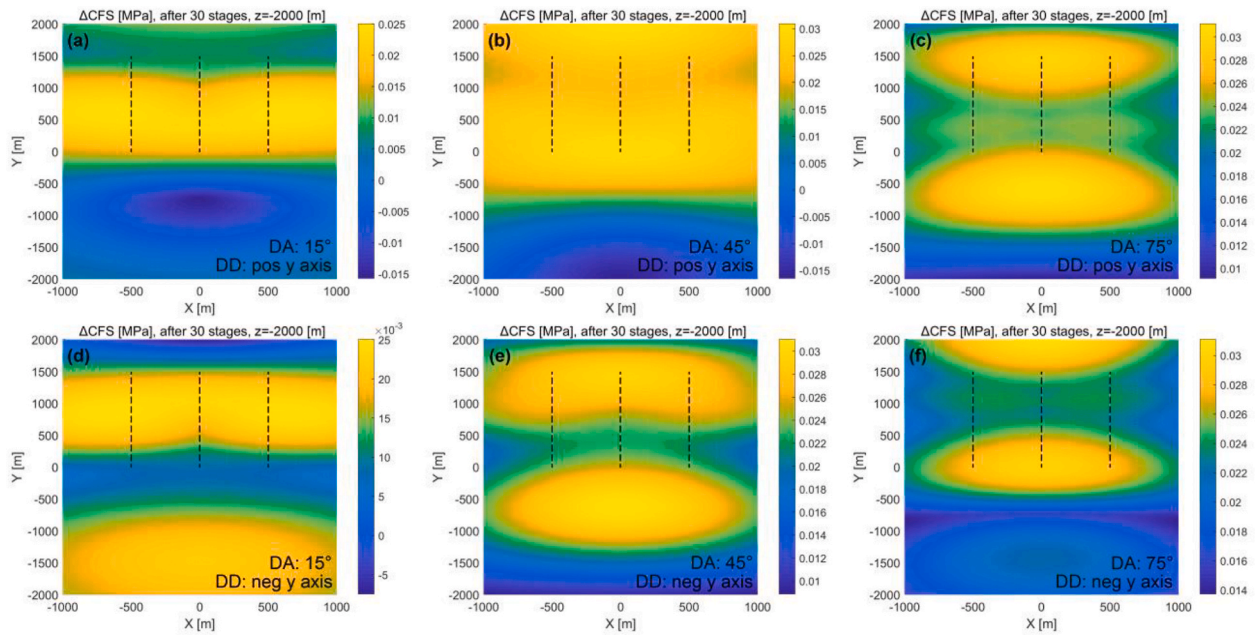


Fig. 15. Contours of Coulomb failure stress (ΔCFS) caused by fracturing of 30 stages in all three wells at a depth of $z = -2$ km. Negative values of z indicate depth below the horizontal fracturing well. DA represents the dip angle and DD denotes the dip direction. Distribution of ΔCFS is shown for the following cases: (a) DA = 15° and DD in the positive y axis, (b) DA = 45° and DD in the positive y axis, (c) DA = 75° and DD in the positive y axis, (d) DA = 15° and DD in the negative y axis, (e) DA = 45° and DD in the negative y axis, and (f) DA = 75° and DD in the negative y axis. The black dashed lines indicate the locations of fracturing wells.

where k_m is the mobility coefficient, defined as the ratio of rock permeability (k) to fluid viscosity (~ 1 cp for slick-water), α denotes the Biot coefficient (~ 0.6), K and G are the drained bulk modulus and shear modulus, respectively. In this, M is the Biot modulus and is expressed as,

$$M = \frac{K_f}{n + (\alpha - n)(1 - \alpha)K_f/K}, \quad (5)$$

where K_f is the fluid bulk modulus (~ 2 GPa for pure water at room temperature) and n represents the porosity of rock matrix. For the Longmaxi shale, the rock matrix exhibits extremely low permeability with the range from 10^{-18} to $10^{-21} m^2$ (e.g., Ref. 24). Considering a characteristic separation of a pre-existing fault from the injection site to be of the order of kms then the characteristic diffusion time (t_c) is in the range of 10^{10} – 10^{13} s or 10^5 to 10^8 d. The fracturing time (t_f) to complete a fracturing pad is assumed to be approximately 1 month ($\sim 3 \times 10^6$ s) and is much lower than the characteristic time (t_c) of diffusion. Therefore, the effects of diffusing pore pressure on the instantaneous stress changes can be neglected due to the low permeability of the rock matrix and the large separation between the injection point and the faults (1–2 km) - the loading is functionally undrained. However, permeability can be greatly increased when pre-existing faults or fractures are encountered. We assume that the effects of pore pressure can be neglected at $t_f/t_c < 0.1$ and we can obtain the permeability (k) under the order of $10^{-15} m^2$ using Eqs. (3)–(5). This indicates that the upper limit of permeability for pre-existing faults or fractures is in the order of $10^{-15} m^2$ to ensure that the system responds as undrained.

5. Conclusions

We define the magnitude and distribution of stress perturbations resulting from first-stage and multistage hydraulic fracturing followed by long term reservoir depletion. A dislocation-based analytical model is utilized to assess the stress perturbations induced by the hydraulic fracturing of a single well pad consisting of three horizontal wells. The stress perturbations are calculated for different number of hydraulic fracturing stages and the implications for fault reactivation potential are

investigated on the basis of a Coulomb failure criterion. The following conclusions are drawn:

1. The stress perturbations induced by the first stage of hydraulic fracturing are relatively small, with magnitudes $\leq 10^{-3} MPa$. For a full completion of thirty fracturing stages on each of three wells on the pad, the magnitudes of the stress perturbations reach $\sim 10^{-2}$ – $10^{-1} MPa$ at a distance of 1 km and reduce to 10^{-3} – $10^{-2} MPa$ at a distance of 2 km. The fracturing stages are shown to affect both the magnitudes and distributions of the stress changes.
2. The fluid-injection-inflated aperture of the individual hydraulic fractures directly influence the stress changes caused by hydraulic fracturing. The induced stress scales with total injection volume and reduces with effective leak-off. Thus, when fracture aperture reduces with time, due to fluid leak-off, this can lower the magnitude of the induced distant stress changes.
3. Both multistage hydraulic fracturing and subsequent reservoir pressure drawdown/depletion result in broadly equivalent stress perturbations at distances of 1 and 2 km. Considering that the effect of depletion is long-term, the impact of short-term multistage hydraulic fracturing on stress changes is more profound.
4. Based on the Coulomb failure criterion, completions involving thirty hydraulic fracturing stages on each of three wells within the pad can induce significant Coulomb failure stresses (ΔCFS), with a magnitude of $\sim 10^{-1} MPa$ at a distance of 1 km and $\sim 10^{-2} MPa$ at a distance of 2 km. This manifests that the stress perturbations resulting from typical multistage hydraulic fracturing operations are sufficient to reactivate pre-existing faults. Our results identify the importance of estimating anticipated stress changes in the evaluation of the induced seismicity hazard for the Changing national shale gas demonstration area of Sichuan Basin and similar sites.

Declaration of competing interest

The authors declare that they have no known competing financial interests or personal relationships that could have appeared to influence the work reported in this paper.

Acknowledgement

This work is supported by the National Key Research and Development Project (No. 2020YFC1808102) and the National Natural Science

Foundation of China (No. 41772286, 41941018, 42077247). We thank Lingyuan Meng for providing the earthquake data of 2017 in Changning area and the data can be found at.⁵

Appendix A. Dislocation Theory for Stress Calculation

Dislocation is a common concept used in material science.^{52–54} It refers to a linear crystallographic defect or irregularity in a crystal structure containing the abrupt change in the arrangement of atoms. The dislocation also defines a boundary between the slipped and unslipped regions within the crystal structure. The major two types of mobile dislocations are the edge (Figure A1a) and screw dislocations. For a regular array of atoms in the crystalline materials, the edge dislocation can be regarded as the termination of a plane of atoms in the middle of the crystal structure (Figure A1a). It will lead to the distortion of nearby atoms and the terminated plane is called the extra half-plane of atoms, as shown in Figure A1a. The joining bonds of atoms will be broken when a sufficiently large force is applied on one side of the crystal structure and finally induces the glide or slippage. In contrast to the edge dislocation, the screw dislocation can be formed by cutting a crystal along a plane and slipping one half across the other. The crystal structure in the screw dislocation is similar to the corner of stairs and a helical path can be traced around the defect.

From the stress computation point of view, the open fractures can be represented as the edge dislocations (Figure A1c). Two elements are important for an edge dislocation. The first element is the dislocation line that extends along the bottom of the extra half-plane of atoms (Figure A1a). Another is the Burgers vector \mathbf{b} that describes the direction and magnitude of the distortion of atom plane.⁵⁵ The Burgers vector is perpendicular to the dislocation line in an edge dislocation (Figure A1a) and can be determined by the Burgers circuits.⁵² The procedures are described as follows. First, we assume that the positive direction of dislocation line points out of the plane of figure. Then, a closed and counterclockwise Burgers circuit $MNPQ$ in the reference crystal (Figure A1b) was formed according to the right-hand rule. In this rule, the thumb points to the positive direction of dislocation line and the four fingers indicate the direction of Burgers circuits. Next, the same circuit $MNPQ$ was plotted on the real crystal with an edge dislocation (Figure A1a). The final vector that closes the Burgers circuit is defined as the Burgers vector \mathbf{b} . In our model, the length of the Burgers vector represents the fracture width.

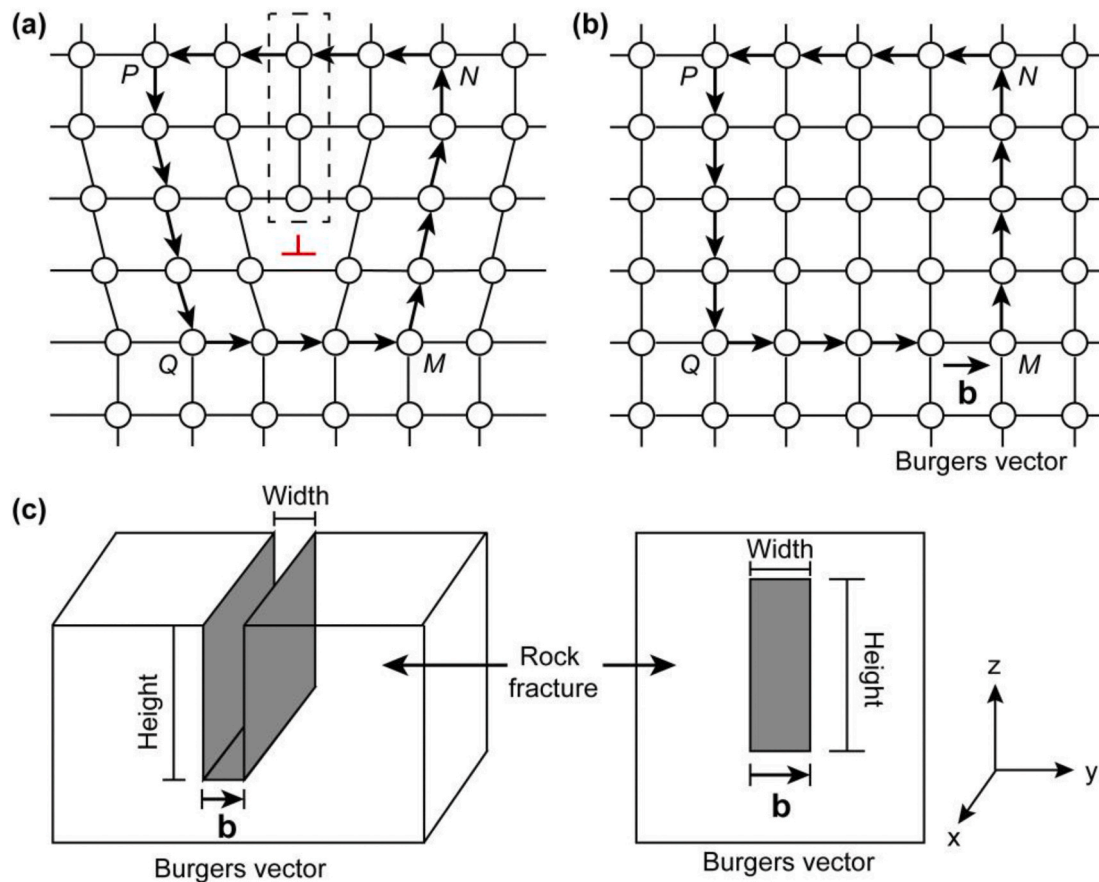


Fig. A1. (a) An example showing an edge dislocation in a crystal (modified from⁵²). The red vertical symbol denotes the dislocation line and points into the paper. The dashed black rectangle indicates the extra half-plane of atoms. (b) An intact crystal given for the reference. The circles represent the atoms in the crystal. (c) A hydraulic fracture can be conceptualized as an edge dislocation and the length of Burgers vector \mathbf{b} is the hydraulic fracture width. The arrangements of the hydraulic fracture and the coordinate system are based on the model in Fig. 4.

The method for calculating the stress variations during hydraulic fracturing using the dislocation theory is described as follows. We consider a rectangular rock fracture ($ABCD$) in the 3D Cartesian coordinate system (Figure A2). The coordinates of the four vertices in the fracture are: $A (-1, 0, -1)$, $B (-1, 0, 1)$, $C (1, 0, 1)$ and $D (1, 0, -1)$, respectively. Then, the effects of fracture deformation and displacement can be considered the same as the influences of displacements of line segments AB , BC , CD and DA on the stress field of any point in space.

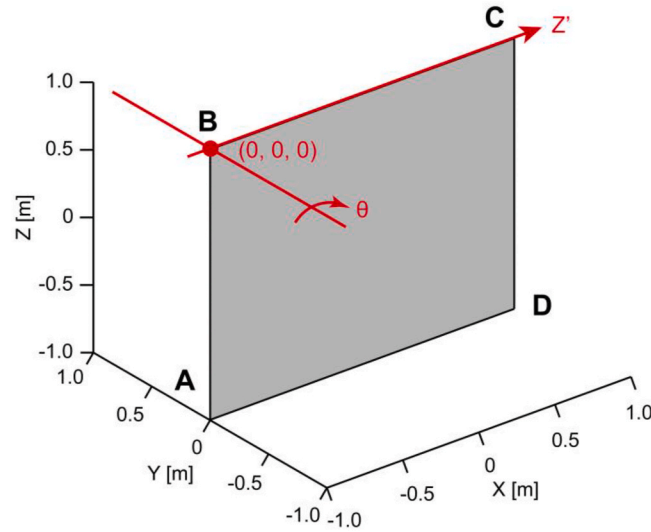


Fig. A2. A rectangular fracture (ABCD) in a 3D Cartesian coordinate system. The red imprints represent the new coordinate system.

All calculations were accomplished on the basis of the dislocation line of Z axis. We take the stress calculation in line segment BC as an example. First, a new coordinate system was established at the origin of point B (0 0 0) and the new Z' axis is along the direction of line BC (Figure A2). A rotation angle θ can be obtained by taking a line parallel to the original Y axis and through point B as the axis of rotation. Next, we compute the rotation matrix \mathbf{R} and the relationship of the coordinates in new coordinate system (x', y', z') and the original coordinate system (x, y, z) is expressed as,

$$\begin{bmatrix} x' \\ y' \\ z' \end{bmatrix} = \mathbf{R}^* \begin{bmatrix} x \\ y \\ z \end{bmatrix} = \begin{bmatrix} R_{11} & R_{12} & R_{13} \\ R_{21} & R_{22} & R_{23} \\ R_{31} & R_{32} & R_{33} \end{bmatrix} * \begin{bmatrix} x \\ y \\ z \end{bmatrix} \quad (6)$$

$$\mathbf{R} = \begin{bmatrix} \cos\theta + u_x^2(1 - \cos\theta) & u_x u_y(1 - \cos\theta) - u_z \sin\theta & u_x u_z(1 - \cos\theta) + u_y \sin\theta \\ u_y u_x(1 - \cos\theta) + u_z \sin\theta & \cos\theta + u_y^2(1 - \cos\theta) & u_y u_z(1 - \cos\theta) - u_x \sin\theta \\ u_z u_x(1 - \cos\theta) - u_y \sin\theta & u_y u_z(1 - \cos\theta) + u_x \sin\theta & \cos\theta + u_z^2(1 - \cos\theta) \end{bmatrix} \quad (7)$$

where (u_x, u_y, u_z) is the unit vector along the Z' axis in the new coordinate system. Then, the stress components ($\sigma_{x'x'}$, $\sigma_{y'y'}$, $\sigma_{z'z'}$, $\sigma_{x'y'}$, $\sigma_{x'z'}$, and $\sigma_{y'z'}$) at any point of the new coordinate system can be calculated as,⁵²

$$\frac{\sigma_{x'x'}}{\sigma_0} = b_x' \frac{y'}{r(r+\lambda)} \left[1 + \frac{x'^2}{r^2} + \frac{x'^2}{r(r+\lambda)} \right] + b_y' \frac{x'}{r(r+\lambda)} \left[1 - \frac{x'^2}{r^2} - \frac{x'^2}{r(r+\lambda)} \right] \quad (8)$$

$$\frac{\sigma_{y'y'}}{\sigma_0} = -b_x' \frac{y'}{r(r+\lambda)} \left[1 - \frac{y'^2}{r^2} - \frac{y'^2}{r(r+\lambda)} \right] - b_y' \frac{x'}{r(r+\lambda)} \left[1 + \frac{y'^2}{r^2} + \frac{y'^2}{r(r+\lambda)} \right] \quad (9)$$

$$\frac{\sigma_{z'z'}}{\sigma_0} = b_x' \left[\frac{y'\lambda}{r^3} + \frac{2\lambda y'}{r(r+\lambda)} \right] + b_y' \left[-\frac{x'\lambda}{r^3} - \frac{2\lambda x'}{r(r+\lambda)} \right] \quad (10)$$

$$\frac{\sigma_{x'y'}}{\sigma_0} = -b_x' \frac{x'}{r(r+\lambda)} \left[1 - \frac{y'^2}{r^2} - \frac{y'^2}{r(r+\lambda)} \right] + b_y' \frac{y'}{r(r+\lambda)} \left[1 - \frac{x'^2}{r^2} - \frac{x'^2}{r(r+\lambda)} \right] \quad (11)$$

$$\frac{\sigma_{x'z'}}{\sigma_0} = -b_x' \frac{x'y'}{r^3} + b_y' \left(-\frac{\nu}{r} + \frac{x'^2}{r^3} \right) + b_z' \frac{y'(1-\nu)}{r(r+\lambda)} \quad (12)$$

$$\frac{\sigma_{y'z'}}{\sigma_0} = b_x' \left(\frac{\nu}{r} - \frac{y'^2}{r^3} \right) + b_y' \frac{x'y'}{r^3} - b_z' \frac{x'(1-\nu)}{r(r+\lambda)} \quad (13)$$

where $\sigma_0 = E/(8\pi * (1 - \nu^2))$, $\lambda = l - z'$, $r^2 = (x')^2 + (y')^2 + (l - z')^2$, E represents the elastic modulus, ν is the Poisson's ratio, l is the length of line segment BC, and b_x' , b_y' and b_z' are calculated as,

$$b_x' = R_{11} * b_1 + R_{12} * b_2 + R_{13} * b_3 \quad (14)$$

$$b_y' = R_{21} * b_1 + R_{22} * b_2 + R_{23} * b_3 \quad (15)$$

$$b_z' = R_{31} * b_1 + R_{32} * b_2 + R_{33} * b_3 \quad (16)$$

where $b_1, b_2,$ and b_3 are the components of the Burgers vector \mathbf{b} ($\mathbf{b} = w * [0 \ 1 \ 0]$). Finally, the stress components σ_{ij} ($i = 1, 2, 3, j = 1, 2, 3$) at the original coordinate system can be obtained by,

$$\sigma_{ij} = R_{mi} * R_{nj} * \sigma_{mn} \tag{17}$$

where σ_{mn} ($m = 1, 2, 3, n = 1, 2, 3$) are the stress components in the new coordinate system. The stress components for the line segments AB, CD and DA are also computed following the above method. The total stress components due to a single rectangular fracture are obtained by the adding the respective stress components for four line segments. Likewise, the total stress from the system of fractures on the pad is evaluated by adding the response from each individual rectangular fracture.

The dislocation approach to compute stress is mathematically equivalent to the commonly used displacement discontinuity method.⁵⁶ To demonstrate this, we consider a simple example of computing normal stress from an infinitesimal rectangular element that is open in the normal direction. With reference to Figure A2, let the element be located at the origin, occupy the xz -plane, and have dimensions dx and dz . The mode of opening is in the y -direction and is equal to w . According to Ref. 56; the stress field in the xz -plane at $y = 0$ is given by

$$\sigma_{yy} = -\sigma_0 \frac{w dx dz}{(x^2 + z^2)^{3/2}} \tag{18}$$

The same expression may be obtained using the dislocation equations outlined above. With reference to Eq. (9), we set $y = 0, b_y = w,$ and $b_x = 0$. Further, to compute contribution of edges AD and BC (noting that they have opposite directions in the dislocation loop), we differentiate Eq. (9) with respect to x and z and select the sign based on the counterclockwise loop direction. Finally, to add the contribution of edges AB and CD , we can utilize symmetry and add a similar expression in which the x and z coordinates are flipped. The result is,

$$\sigma_{yy} = \sigma_0 w dx dz \frac{\partial}{\partial x} \frac{\partial}{\partial z} \left(\frac{x}{R(R-z)} + \frac{z}{R(R-x)} \right), \quad R^2 = x^2 + z^2 \tag{19}$$

Noting that $\partial R / \partial x = x/R$ and $\partial R / \partial z = z/R$, after some manipulation, the expression for stress is identical to that outlined above from the displacement discontinuity approach. Similarly, the mathematical equivalence between the dislocation and the displacement discontinuity approaches can be demonstrated for all other stress components and components of Burgers vector. We have checked the equivalence between the two approaches for all stress components.

Appendix B. Poroelastic Theory for Stress Calculation

The stress components σ_{ij} in the cuboid depletion zone can be quickly estimated by,³⁹

$$\sigma_{ij} = \frac{\alpha p(1-2\nu)}{1-\nu} \left(\delta_{ij} + \frac{1}{4\pi} I_{ij} \right) \tag{20}$$

where α is the Biot coefficient, p represents the change of the pore pressure, δ_{ij} is the Kronecker delta, ν denotes the Poisson's ratio, the integral of the potential can be expressed as,

$$I(x, y, z) = \int_{x-a}^{x+a} \int_{y-b}^{y+b} \int_{z-c}^{z+c} \frac{dx' dy' dz'}{\sqrt{(x-x')^2 + (y-y')^2 + (z-z')^2}} \tag{21}$$

Derivatives of the potential (21) that enter Eq. (20) are calculated as,

$$I_{,ij}(x, y, z) = \widehat{I}_{,ij}(x+a, y+b, z+c) - \widehat{I}_{,ij}(x-a, y+b, z+c) - \widehat{I}_{,ij}(x+a, y-b, z+c) + \widehat{I}_{,ij}(x-a, y-b, z+c) - \widehat{I}_{,ij}(x+a, y+b, z-c) + \widehat{I}_{,ij}(x-a, y+b, z-c) + \widehat{I}_{,ij}(x+a, y-b, z-c) - \widehat{I}_{,ij}(x-a, y-b, z-c), \tag{22}$$

where

$$\widehat{I}_{,xx} = -\tan^{-1} \left(\frac{yz}{xr_d} \right), \widehat{I}_{,yy} = -\tan^{-1} \left(\frac{xz}{yr_d} \right), \widehat{I}_{,zz} = -\tan^{-1} \left(\frac{xy}{zr_d} \right), \tag{23}$$

$$\widehat{I}_{,yz} = \log(x+r_d), \widehat{I}_{,xz} = \log(y+r_d), \widehat{I}_{,xy} = \log(z+r_d),$$

$$\text{and } r_d^2 = x^2 + y^2 + z^2.$$

Appendix C. Supplementary data

Supplementary data to this article can be found online at <https://doi.org/10.1016/j.ijrmms.2021.104704>.

References

1 Atkinson GM, Eaton DW, Igonin N. Developments in understanding seismicity triggered by hydraulic fracturing. *Nat Rev Earth Environ*. 2020;1(5):264–277. <https://doi.org/10.1038/s43017-020-0049-7>.

2 Lei X, Huang D, Su J, et al. Fault reactivation and earthquakes with magnitudes of up to M_w 4.7 induced by shale-gas hydraulic fracturing in Sichuan Basin, China. *Sci Rep*. 2017;7:7971. <https://doi.org/10.1038/s41598-017-08557-y>.

3 Lei X, Wang Z, Su J. The December 2018 M_L 5.7 and January 2019 M_L 5.3 earthquakes in south Sichuan Basin induced by shale gas hydraulic fracturing. *Seismol Res Lett*. 2019;90(3):1099–1110. <https://doi.org/10.1785/0220190029>.

- 4 Liu J, Zahradník J. The 2019 M_w 5.7 Changning earthquake, Sichuan Basin, China: a shallow doublet with different faulting styles. *Geophys Res Lett.* 2020;47(4). <https://doi.org/10.1029/2019GL085408>.
- 5 Meng L, McGarr A, Zhou L, Zang Y. An investigation of seismicity induced by hydraulic fracturing in the Sichuan Basin of China based on data from a temporary seismic network. *Bull Seismol Soc Am.* 2019;109(1):348–357. <https://doi.org/10.1785/0120180310>.
- 6 Zhang F, An M, Zhang L, Fang Y, Elsworth D. The role of mineral composition on the frictional and stability properties of powdered reservoir rocks. *J Geophys Res Solid Earth.* 2019;124:1480–1497. <https://doi.org/10.1029/2018JB016174>.
- 7 Tuo J, Wu C, Zhang M. Organic matter properties and shale gas potential of Paleozoic shales in Sichuan Basin, China. *J Nat Gas Sci Eng.* 2016;28:434–446. <https://doi.org/10.1016/j.jngse.2015.12.003>.
- 8 Zou C, Dong D, Wang S, et al. Geological characteristics and resource potential of shale gas in China. *Petrol Explor Dev.* 2010;37(6):641–653. [https://doi.org/10.1016/S1876-3804\(11\)60001-3](https://doi.org/10.1016/S1876-3804(11)60001-3).
- 9 Bao X, Eaton DW. Fault activation by hydraulic fracturing in western Canada. *Science.* 2016;354(6318):1406–1409. <https://doi.org/10.1126/science.aag2583>.
- 10 Elsworth D, Spiers CJ, Niemeijer AR. Understanding induced seismicity. *Science.* 2016;354(6318):1380–1381. <https://doi.org/10.1126/science.aal2584>.
- 11 Rubinstein JL, Mahani AB. Myths and facts on wastewater injection, hydraulic fracturing, enhanced oil recovery, and induced seismicity. *Seismol Res Lett.* 2015;86(4):1060–1067. <https://doi.org/10.1785/0220150067>.
- 12 Schultz R, Atkinson G, Eaton DW, Gu YJ, Kao H. Hydraulic fracturing volume is associated with induced earthquake productivity in the duvernay play. *Science.* 2018;359(6373):304–308. <https://doi.org/10.1126/science.aao0159>.
- 13 Chang KW, Segall P. Injection-induced seismicity on basement faults including poroelastic stressing. *J Geophys Res: Solid Earth.* 2016;121(4):2708–2726. <https://doi.org/10.1002/2015JB012561>.
- 14 Davies R, Foulger G, Bindley A, Styles P. Induced seismicity and hydraulic fracturing for the recovery of hydrocarbons. *Mar Petrol Geol.* 2013;45:171–185. <https://doi.org/10.1016/j.marpetgeo.2013.03.016>.
- 15 Shapiro SA, Dinske C. Fluid-induced seismicity: pressure diffusion and hydraulic fracturing. *Geophys Prospect.* 2009;57(2):301–310. <https://doi.org/10.1111/j.1365-2478.2008.00770.x>.
- 16 Yang Y-H, Hu J-C, Chen Q, et al. Shallow slip of blind fault associated with the 2019 M_s 6.0 Changning earthquake in fold-and-thrust belt in salt mines of Southeast Sichuan, China. *Geophys J Int.* 2020;224(2):909–922. <https://doi.org/10.1093/gji/ggaa488>.
- 17 Ellsworth WL, Townend J, Zoback MD, et al. Injection-induced earthquakes. *Science.* 2013;341(642), 1225942. <https://doi.org/10.1126/science.1225942>.
- 18 Fang Y, Elsworth D, Cladouhos TT. Reservoir permeability mapping using microearthquake data. *Geothermics.* 2018;72:83–100. <https://doi.org/10.1016/j.geothermics.2017.10.019>.
- 19 Hough SE. Shaking from injection-induced Earthquakes in the central and eastern United States. *Bull Seismol Soc Am.* 2014;104(5):2619–2626. <https://doi.org/10.1785/0120140099>.
- 20 Kim KH, Ree JH, Kim YH, Kim S, Kang SY, Seo W. Assessing whether the 2017 M_w 5.4 Pohang earthquake in South Korea was an induced event. *Science.* 2018;360(6392):1007–1009. <https://doi.org/10.1126/science.aat6081>.
- 21 Suckale J. Induced seismicity in hydrocarbon fields. *Adv Geophys.* 2009;51:55–106. [https://doi.org/10.1016/S0065-2687\(09\)05107-3](https://doi.org/10.1016/S0065-2687(09)05107-3).
- 22 Eyre TS, Eaton DW, Garagash DI, et al. The role of aseismic slip in hydraulic fracturing-induced seismicity. *Sci Adv.* 2019;5(8), eaav7172. <https://doi.org/10.1126/sciadv.aav7172>.
- 23 Liang C, Jiang Z, Zhang C, Guo L, Yang Y, Li J. The shale characteristics and shale gas exploration prospects of the Lower Silurian longmaxi shale, Sichuan Basin, South China. *J Nat Gas Sci Eng.* 2014;21:636–648. <https://doi.org/10.1016/j.jngse.2014.09.034>.
- 24 Zhou J, Zhang L, Li X, Pan Z. Experimental and modeling study of the stress-dependent permeability of a single fracture in shale under high effective stress. *Fuel.* 2019;257, 116078. <https://doi.org/10.1016/j.fuel.2019.116078>.
- 25 Eaton DW. *Passive Seismic Monitoring of Induced Seismicity: Fundamental Principles and Application to Energy Technologies.* Cambridge University Press; 2018.
- 26 Chen J, Verberne BA, Spiers CJ. Interseismic re-strengthening and stabilization of carbonate faults by “non-Dieterich” healing under hydrothermal conditions. *Earth Planet Sci Lett.* 2015;423:1–12. <https://doi.org/10.1016/j.epsl.2015.03.044>.
- 27 Hunfeld LB, Niemeijer AR, Spiers CJ. Frictional properties of simulated fault gouges from the seismogenic groningen gas field under in situ P-T-chemical conditions. *J Geophys Res Solid Earth.* 2017;122(11). <https://doi.org/10.1002/2017JB014876>.
- 28 Pluyackers AMH, Samuelson JE, Niemeijer AR, Spiers CJ. Effects of temperature and CO_2 on the frictional behavior of simulated anhydrite fault rock. *J Geophys Res: Solid Earth.* 2014. <https://doi.org/10.1002/2014JB011575>.
- 29 Xu Z, Jiang S, Yao G, Liang X, Xiong S. Tectonic and depositional setting of the lower Cambrian and lower Silurian marine shales in the Yangtze Platform, South China: implications for shale gas exploration and production. *J Asian Earth Sci.* 2019. <https://doi.org/10.1016/j.jseas.2018.10.023>.
- 30 Keranen KM, Weingarten M, Abers GA, Bekins BA, Ge S. Sharp increase in central Oklahoma seismicity since 2008 induced by massive wastewaters injection. *Science.* 2014;345(6195):448–451. <https://doi.org/10.1126/science.1255802>.
- 31 Goebel THW, Weingarten M, Chen X, Haffener J, Brodsky EE. The 2016 M_w 5.1 Fairview, Oklahoma earthquakes: evidence for long-range poroelastic triggering at >40 km from fluid disposal wells. *Earth Planet Sci Lett.* 2017;472:50–61. <https://doi.org/10.1016/j.epsl.2017.05.011>.
- 32 Kettlety T, Verdon JP, Werner MJ, Kendall JM, Budge J. Investigating the role of elastostatic stress transfer during hydraulic fracturing-induced fault activation. *Geophys J Int.* 2019;217(2):1200–1216. <https://doi.org/10.1093/gji/ggz080>.
- 33 Sumy DF, Cochran ES, Keranen KM, Wei M, Abers GA. Observations of static Coulomb stress triggering of the November 2011 M_s 5.7 Oklahoma earthquake sequence. *J Geophys Res: Solid Earth.* 2014;119(3):1904–1923. <https://doi.org/10.1002/2013JB010612>.
- 34 King GCP, Stein RS, Lin Jian. Static stress changes and the triggering of earthquakes. *Bull Seismol Soc Am.* 1994;84(3):935–953. [https://doi.org/10.1016/0148-9062\(95\)94484-2](https://doi.org/10.1016/0148-9062(95)94484-2).
- 35 Harris RA. Introduction to special section: stress triggers, stress shadows, and implications for seismic hazard. *J Geophys Res: Solid Earth.* 1998;103(B10):24347–24358. <https://doi.org/10.1029/98jb01576>.
- 36 Stein RS. The role of stress transfer in earthquake occurrence. *Nature.* 1999;402(6762):605–609. <https://doi.org/10.1038/45144>.
- 37 Toda S, Stein RS. Did stress triggering cause the large off-fault aftershocks of the 25 March 1998 M_w = 8.1 Antarctic plate earthquake? *Geophys Res Lett.* 2000;27(15):2301–2304. <https://doi.org/10.1029/1999GL011129>.
- 38 Chen H, Meng X, Niu F, Tang Y, Yin C, Wu F. Microseismic monitoring of stimulating shale gas reservoir in SW China: 2. Spatial clustering controlled by the preexisting faults and fractures. *J Geophys Res: Solid Earth.* 2018;123(2):1659–1672. <https://doi.org/10.1002/2017JB014491>.
- 39 Dontsov EV. An efficient computation of leak-off induced poroelastic stress for a hydraulic fracture. *J Mech Phys Solid.* 2021;147, 104246.
- 40 Addis MA. Reservoir depletion and its effect on wellbore stability evaluation. *Int J Rock Mech Min Sci Geomech Abstr.* 1997;34(3–4):423. [https://doi.org/10.1016/S1365-1609\(97\)00238-4](https://doi.org/10.1016/S1365-1609(97)00238-4).
- 41 Liu S, Harpalani S. Evaluation of in situ stress changes with gas depletion of coalbed methane reservoirs. *J Geophys Res: Solid Earth.* 2014;119(8):6263–6276. <https://doi.org/10.1002/2014JB011228>.
- 42 Detournay E, Cheng AHD. Fundamentals of poroelasticity. In: Hudson JA, ed. *Comprehensive Rock Engineering.* vol. 2. London: Pergamon Press; 1993:113–171.
- 43 Zoback MD. *Reservoir Geomechanics.* New York: Cambridge University Press; 2007.
- 44 Nowacki W. *Theory of Asymmetric Elasticity.* New York: Pergamon Press; 1986.
- 45 Zhang JJ. *Applied Petroleum Geomechanics.* Gulf Professional Publishing; 2019.
- 46 Brodsky EE, Prejlec SG. New constraints on mechanisms of remotely triggered seismicity at Long Valley Caldera. *J Geophys Res: Solid Earth.* 2005;110(B4). <https://doi.org/10.1029/2004JB003211>.
- 47 Deng K, Liu Y, Harrington RM. Poroelastic stress triggering of the December 2013 Crooked Lake, Alberta, induced seismicity sequence. *Geophys Res Lett.* 2016;43(16):8482–8491. <https://doi.org/10.1002/2016GL070421>.
- 48 Lockner DA, Beeler NM. Premonitory slip and tidal triggering of earthquakes. *J Geophys Res: Solid Earth.* 1999;104(B9):20133–20151. <https://doi.org/10.1029/1999JB900205>.
- 49 An M, Zhang F, Elsworth D, Xu Z, Chen Z, Zhang L. Friction of Longmaxi shale gouges and implications for seismicity during hydraulic fracturing. *J Geophys Res: Solid Earth.* 2020;125, e2020JB019885. <https://doi.org/10.1029/2020JB019885>.
- 50 Biot M. General solutions of the equation of elasticity and consolidation for a porous material. *J Appl Mech.* 1956;23(1):91–96.
- 51 Carslaw HS, Jaeger JC. *Conduction of Heat in Solids.* second ed. Oxford: the Calderon Press; 1959.
- 52 Hirth JP, Lothe J. *Theory of Dislocations.* New York: Wiley; 1982.
- 53 Hull D, Bacon DJ. *Introduction to Dislocations.* Oxford: Butterworth-Heinemann; 2001.
- 54 Taylor GI. The mechanism of plastic deformation of crystals. Part I.—Theoretical. *Proc R Soc Lond - Ser A Contain Pap a Math Phys Character.* 1934;145(855):362–387. <https://doi.org/10.1098/rspa.1934.0106>.
- 55 Burgers JM. Physics.—some considerations on the fields of stress connected with dislocations in a regular crystal lattice. In: *Selected Papers of JM Burgers.* Dordrecht: Springer; 1995:335–389.
- 56 Crouch SL, Starfield AM. *Boundary Element Methods in Solid Mechanics.* London: George Allen and Unwin; 1983.
- 57 Zhang F, Yin Z, Chen Z, Maxwell S, Zhang L, Wu Y. Fault reactivation and induced seismicity during multistage hydraulic fracturing: microseismic analysis and geomechanical modeling. *SPE J.* 2019;25(2). <https://doi.org/10.2118/199883-PA>.